

www.acsanm.org Article

Ionic-like Superlattices by Charged Nanoparticles: A Step Toward Photonics Applications

Binay P. Nayak, Honghu Zhang, Wei Bu, Benjamin M. Ocko, Alex Travesset, David Vaknin, Surya K. Mallapragada,* and Wenjie Wang*



Cite This: ACS Appl. Nano Mater. 2024, 7, 3220-3228



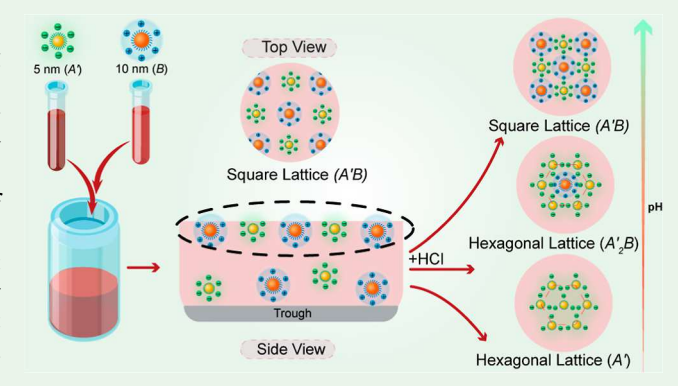
ACCESS I

III Metrics & More

Article Recommendations

SI Supporting Information

ABSTRACT: Controlling interactions among nanoparticles is paramount to achieving assemblies vital to technologies seeking to exploit their cutting-edge collective properties. Although various techniques have been advanced, robust ones are necessary for upscaling nanoparticle assembly and crystallization. Here, we show that by grafting gold nanoparticles (AuNPs) with charge-endgroup-thiolated poly(ethylene glycol), we control the charge of each AuNP. Such control facilitates the formation of various two-dimensional structures of oppositely charged binary constituents at vapor/liquid interfaces. Using surface-sensitive synchrotron X-ray diffraction techniques, we established the formation of distinct checkerboard square lattice structures at a range of pH values and molar ratios of the constituents. By regulating pH, the superlattices



can transform from a square to a hexagonal lattice, or vice versa, and to a single-component superstructure at the interface. Our recipe for the control of charges and their consequent interactions among nanoparticles can be readily exploited in the assembly of photonics and plasmonics devices in two and three dimensions.

KEYWORDS: charge-polymer-grafted nanoparticles, binary ionic-like superstructures, X-ray diffraction, phase-transformations, superstructures

1. INTRODUCTION

Recent advancements in the self-assembly of metallic nanostructures into ordered lattices have garnered significant attention by virtue of their potential applications in optoelectronics, 1,2 plasmonics, 3-5 photonics, 6,7 catalysis, 8,9 and energy storage devices. 10,11 Binary nanoparticle superlattices (BNSLs), consisting of individual nanoparticles that mimic atoms, add a plethora of unique structures with the desired properties sought for these applications. 12-19 Surface grafting of nanoparticles with ligands (e.g., alkyl chains, ss-DNA, polymers, etc.) is commonly used to mediate interparticle interactions in a suitable solvent to achieve assembly and crystallization. 14,17,20-23 Recent studies have achieved the assembly of small (~4 nm) gold nanoparticles (AuNPs) through micelle or covalent bond induction, particularly under conditions of extreme nanoparticle densification. 24,25 Furthermore, the construction of multicomponent BNSLs in both two- and three-dimensional arrays has been successfully demonstrated using polymer-grafted inorganic spherical NPs. 26 Coulombic interactions have been employed to assemble AuNPs (~5 nm) grafted with short positively charged ligands using charged molecules in aqueous solution after multiple separation processes from organic solvents.²⁷ In addition, ferritin-coated anionic protein cages have been

assembled into large crystallites using electrostatic interaction induced by adding cationic dendrimers. ^{23,28}

Here, we explore the self-assembly of charged BNSLs at vapor/liquid interfaces by grafting AuNPs with poly(ethylene glycol) (PEG) terminated with either –COOH or –NH₂ groups. The advantage of this method lies in its ability to manipulate surface charges on the particles, thereby facilitating targeted assembly. However, the challenge lies in fine-tuning the interactions to ensure precise control over the assembled superstructures. In order to achieve the novel desired BNSLs, we control the charge of each nanoparticle (referred to as "superion") by manipulating the pH of the aqueous suspensions and the mixing ratios of the constituents. Theoretical models demonstrate that the dissociation behavior of charge-terminated NPs is influenced by the size and surface curvature of the nanoparticles, as well as by the presence of counterions in the surrounding medium. These factors

Received: November 21, 2023 Revised: January 2, 2024 Accepted: January 4, 2024 Published: January 29, 2024





Table 1. Summary of Notations for AuNPs Used in This Study with Their Hydrodynamic Size and ζ-Potential Values^a

End group of grafted PEG	Diameter of AuNPs $(nm)^b$	Symbolic notation used	Illustrative notation used	Hydrodynamic size $(nm)^e$	рН	ζ potential (mV)
n.a. ^c	10	n.a.		17.0(2)	\sim 5.7	-40.5 ± 1.9
-СООН	10	A		39.5(2)	\sim 5.8	-35.7 ± 1.4
$-NH_2$	10	В		$57.7(4)^d$	~8.1	$+23.0 \pm 1.9$
$\mathrm{n.a.}^{c}$	5	n.a.		10.1(23)	~ 5.5	-30.4 ± 3.9
-COOH	5	A'		34.0(4)	\sim 5.3	-33.3 ± 2.1
-NH ₂	5	B'		$40.0(4)^d$	~7.8	$+11.6 \pm 1.2$
Description of the last of the	·					<u> </u>



^aColumns 3 and 4summarize all the symbolic and illustrative notations used for AuNPs in the article. Columns 5, 6, and 7 summarize the corresponding nanoparticles' hydrodynamic size, pH values, and ζ -potential values. ^bThe diameter is from the vendor. ^cThe bare-surface AuNPs are stabilized with citrate ligands. ^dOnly the diffusional component of the DLS size is reported. Refer to Supporting Information for a detailed discussion. ^eOnly the modal size on the distribution profile is reported.

collectively affect the apparent acid dissociation constant (p $K_{\rm a}$) of the grafted NP, which lies between that of free ligands and ligands assembled on a flat surface. In previous studies, it has been shown that BNSLs can be created by mixing chargeneutral PEG-grafted AuNPs with two different molecular weights of PEG. We use AuNPs of nominal core size, 5 and 10 nm, to enhance electron-density contrast between the two \sim 5 kDa-PEG-grafted particles.

We hypothesize that oppositely charged PEG-grafted AuNPs, acting as superions, form ionic superlattices akin to ionic crystals. Unlike these ionic crystals, this approach allows for the manipulation of the relative surface charge between the two constituents. The relative charge on each particle is tuned by the manipulation of the pH of the suspension. We note that the net charge of a nanoparticle is substantially influenced by the charge of the terminal group³⁰ and the residual charge inherent to the AuNPs.^{31,32} Three key interactions mediate the population and crystallization at the interface: the hydrophobic and van der Waals interactions among PEG chains and the Coulombic interactions due to the charged terminals.

Here, we employ surface-sensitive synchrotron-based X-ray diffraction methods to determine the crystal structures of BNSLs at the vapor/liquid interface. The surface assembly approach has been used extensively with liquid-surface diffractometers, both at X-ray synchrotron facilities and labbased diffractometers, as described in detail in refs 14, 33–35. Our findings reveal intriguing pseudostoichiometries and novel symmetries present for the charged BNSLs, which are distinct from those observed in neutral PEG systems. 14,35,36,41

2. METHODS

2.1. Materials Preparations. Unconjugated citrate-capped bare AuNPs (nominal core diameters of 5 and 10 nm) were purchased from Ted Pella Inc., and their size distributions were independently validated by small-angle X-ray scattering. ^{14,34} PEG of average molecular weight 5 kDa, with one end terminated with thiol (SH)

and the other terminated with either amine(-NH2) or carboxyl(-COOH), was purchased from Creative PEGworks (NC, USA). AuNPs were functionalized with HS-PEG-COOH or HS-PEG- NH_2 by the ligand exchange method, as described below. 14,36 PEG ligands were first dissolved in a 1 M sodium chloride (NaCl) solution and mixed thoroughly. An excess amount of PEG-NaCl solution was mixed with AuNPs using specific ratios: 1 part of 10 nm AuNPs to 6000 parts PEG and 1 part of 5 nm AuNPs to 1500 parts PEG.³⁶ The pH of 5 and 10 nm suspensions was measured as approximately at 5.5 and 5.7, respectively. The resulting mixture was incubated for at least 24 h with continuous mixing with a Roto-Shake Genie (Scientific Industries, NY, USA). The unbound PEG in the PEG-grafted AuNPs suspension was removed by centrifugation three times at 21,000 RCF for 90 min. In this study, the term PEG-AuNP represents PEGgrafted AuNPs in general, while x-PEG-AuNPy indicates AuNPs of y core diameter (i.e., y = 10 or 5 nm) terminated with the x group (i.e., x = -COOH or $-NH_2$ groups) of PEG. For instance, COOH-PEG-AuNP10 refers to AuNPs of an average diameter of 10 nm, functionalized with carboxyl-terminated PEG. For convenience, we represent each grafted nanoparticle as shown by letters and symbols in Table 1. The final concentration of the PEG-AuNPs was determined by measuring their absorbance using ultraviolet-visible (UV-vis) spectroscopy (NanoDrop One Microvolume instrument from Thermo Fischer Scientific) and then adjusted to ~15 and ~60 nM for 10 and 5 nm nanoparticles, respectively. Subsequently, the hydrodynamic diameter (D_H) of the grafted nanoparticles was determined using dynamic light scattering (DLS) with a NanoZS90 and its associated software Zetasizer (Malvern, United Kingdom). To quantify the surface charge of the PEG-grafted AuNPs, ζ -potential measurements were conducted by using the NanoZS90 instrument. The results of these measurements are listed in Tables 1 and S1 and Figure S1. The grafting density of the PEG-AuNPs can be found in a published article (ref 30). The COOH-PEG-AuNPs and NH2-PEG-AuNPs were characterized by opposite electrical charges and enlarged hydrodynamic sizes, indicating the successful grafting of PEG with distinct terminal groups. More detailed information on PEG grafting and characterization is provided in the Supporting Information and a previously published article.³

Table 2. Summary of GISAXS Analysis Based on Data Collected at the APS and NSLS-II for the Binary Mixture of Charged AuNPs^a

AuNP size (nm)		mixing ratio	[HCl] (mM)	lattice type (stoichiometry)		unit cell edge length $a (nm)^b$	
COOH-PEG	NH ₂ -PEG						
A'	В	A'/B					
5	10	1:1	0	$\sqrt{2} \times \sqrt{2}$	square $(A'B)$	49.6 ± 2.3	
			0.1	$\sqrt{2} \times \sqrt{2}$	square $(A'B)$	47.3 ± 2.1	
			1	$\sqrt{2} \times \sqrt{2}$	square $(A'B)$	45.3 ± 2.0	
			10	1×1	hexagonal (likely A')	31.5 ± 1.2	
5	10	2:1	0	$\sqrt{2} \times \sqrt{2}$	square $(A'B)$	50.9 ± 2.5	
			0.1	$\sqrt{2} \times \sqrt{2}$	square $(A'B)$	43.3 ± 1.8	
			1	$\sqrt{3} \times \sqrt{3}$	hexagonal $(A_2'B)$	49.3 ± 1.6	
			10	1×1	hexagonal (likely A')	28.5 ± 1.0	
5	10	4:1	0				
			0.1				
			1	$\sqrt{3} \times \sqrt{3}$	hexagonal $(A_2'B)$	53.2 ± 1.9	
		mixing ratio	10		SRO	,	
AuNP size	AuNP size (nm)		[HCl] (mM)	lattice type (stoichiometry)		unit cell edge length $a (nm)^b$	
COOH-PEG	NH ₂ -PEG						
A	B'	A/B'					
10	5	1:1	0				
			0.1				
			1	$\sqrt{3} \times \sqrt{3}$	hexagonal (AB_2')	54.6 ± 2.0	
			10	1×1	hexagonal (likely A)	30.5 ± 1.1	
10	5	1:2	0				
			0.1		()		
			1	$\sqrt{2} \times \sqrt{2}$	square (AB')	38.6 ± 1.4	
	_		10	1 × 1	hexagonal (likely A)	29.3 ± 1.0	
10	5	1:4	0				
			0.1	/a v /a	Gaussia (API)	41 6 1 17	
			1	$\sqrt{2} \times \sqrt{2}$	square (AB')	41.6 ± 1.7	
			10	$\sqrt{3} \times \sqrt{3}$	MRO hexagonal (uncertain)	54.7 ± 2.0	

"GISAXS suggests LRO for most of the structures, while SRO and MRO are observed in a few cases. Refer to Supporting Information for more details. For the 2D 1 × 1 hexagonal structure, lattice constant $a = 4\pi/(\sqrt{3} Q_{10})$; for the 2D $\sqrt{3} \times \sqrt{3}$ hexagonal structure, lattice constant $a = 4\pi/(Q_{11})$; and for the 2D square structure, lattice constant $a = 2\sqrt{2}\pi/Q_{11}$. The error-bar estimation is described in the Supporting Information section.

For the liquid surface X-ray diffraction experiments, the nanoparticle suspensions were mixed in the desired molar ratio and incubated for approximately 15 min before loading onto a stainless steel trough. The trough with the sample was contained in an enclosed sample chamber purged with water-saturated helium on the X-ray liquid surface spectrometer. A calculated amount of stock HCl solution was added incrementally to the same mixture suspension for a sequence of target pH values and incubated for about 20 min before X-ray measurements. It should be noted that changing the pH is entangled with the ionic strength. A schematic representation of the working method is represented in Figure 1.

2.2. X-ray Diffraction Measurements. Synchrotron-based *insitu* liquid surface X-ray scattering experiments were performed at NSF's ChemMatCARS Sector 15, Advanced Photon Source, Argonne National Laboratory, and at SMI beamline open platform liquid surfaces (OPLS) end station, National Synchrotron Light Source II (NSLS-II), Brookhaven National Laboratory, with incident X-ray energies of 10 and 9.7 keV, respectively. Liquid-surface specular X-ray reflectivity (XR) and grazing incidence small-angle X-ray scattering (GISAXS) were conducted to determine the density profile across the vapor/liquid interface and the in-plane arrangement of nanoparticle assembly at the aqueous surface. The experimental instrumental setup and measurement protocols at these two beamlines are detailed in previous reports. ^{5,14,36,39}

Below is a brief description of the data collection and presentation. Incident X-rays of the wavevector \vec{k}_i were incident upon the aqueous surface at grazing angles, and scattered X-rays of the wavevector k_f were recorded using an area detector, where the scattering intensity was recorded as a function of the scattering vector \vec{Q} , $\vec{Q} = \vec{k_f} - \vec{k_i}$. Q_z and Q_{xy} denote the vertical and horizontal components of \vec{Q} , respectively. The scattered intensities in GISAXS are presented as 2D images in terms of Q_{xy} and Q_z . All the GISAXS 2D images (Q_z vs Q_{xy}) are provided in the Supporting Information: Figures S2-S5. A linecut intensity profile of GISAXS as a function of Qxy is integrated over the Q_z range 0.01-0.03 Å⁻¹ (see Figure S2), denoted as $I(Q_{xy})$. The diffraction peaks are marked with Miller indices (h, k) for the identified 2D lattice type. GISAXS linecut intensity profiles for controlled GISAXS measurements on PEG-AuNPs of each size are provided in Figures S6-S8. Two-dimensional structure factor considerations based on GISAXS are illustrated in Figure S9. Examples of linecut intensity profiles for long-range order (LRO), meso-range order (MRO), and short-range order (SRO) are provided in Figure S10. For XR, the reflectivity $R(Q_z)$ was normalized to the Fresnel reflectivity, R_F, calculated for the corresponding ideal flat surface solutions. The electron density (ED) profiles along the vertical direction z, $\rho(z)$, were obtained using Parratt's recursive method from

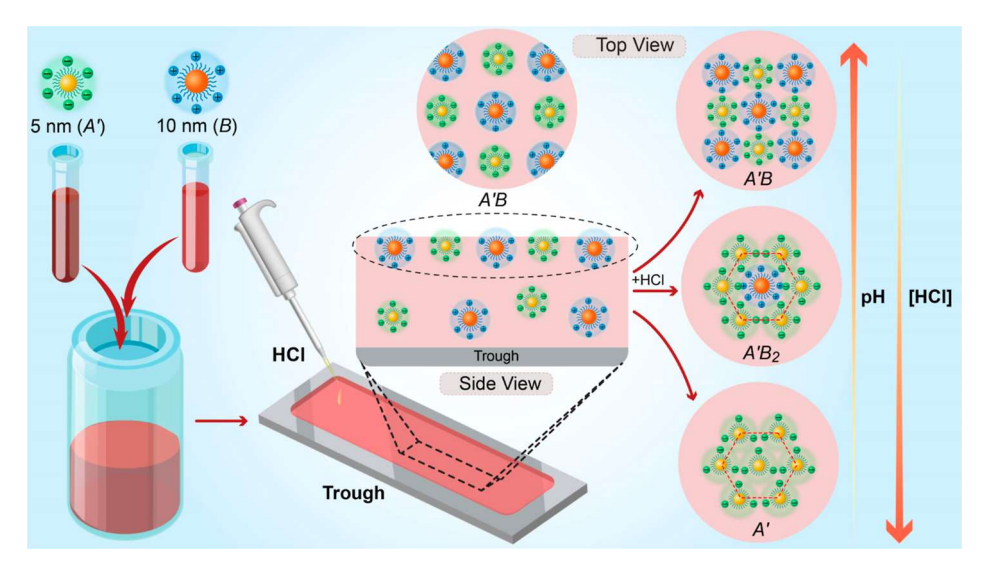


Figure 1. Schematic illustration of lattice transition and experimental procedure. The two vials contain suspensions of AuNPs that are grafted with thiolated PEG and terminated with either $-NH_2$ or -COOH. The core (5 or 10 nm) is chosen to enhance the X-ray scattering contrast between the two constituents. The two constituents are mixed with a desired molar mixing ratio into a secondary vial and spread into a stainless-steel trough. Surface-sensitive X-ray scattering, including XR and GISAXS, is conducted on the filled-trough surface. By adjusting the pH and molar-mixing ratio, we obtain various structures, including checkerboard-like and binary hexagonal structures, as summarized in Figure 5.

fitted R/R_F data.⁴⁰ Detailed XR analysis is demonstrated in the Supporting Information, including Figures S11–S15 and Table S3.

3. RESULTS AND DISCUSSION

3.1. Charge-Balanced Superstructures. We begin by investigating the mixtures of 1:1 molar ratio of oppositely charged particles, symbolically (A and B') and (A' and B) (see Table 1 for nomenclatures). We note that at neutral pH, the net charge per particle differs according to the specific PEG end group; manipulating the pH controls the net charge per particle and the resultant superstructure. At near-neutral pH, the (A/B') system does not exhibit an accumulation of particles at the interface. In contrast, (A'/B) exhibits surface accumulation with the formation of a square lattice at a SRO. This finding is also based on XR analysis, which shows the presence of AuNPs at the surface (see Figures S7, S8, and S11 and the detailed discussion on SRO in Supporting Information). To balance the charges on the NPs, we lowered the pH values from neutral to as low as pH 2. Intriguingly, for both the A'/B and A/B' systems, we observe two novel structures at pH 3, as shown in Figure 2. Figure 2a shows a 1D diffraction pattern (see Methods) of the (A'/B) with Bragg peaks that can be indexed by a $\sqrt{2} \times \sqrt{2}$ square lattice with the unit cell edge $a \simeq 50$ nm. This notation (i.e., $\sqrt{2} \times \sqrt{2}$) is used to indicate that the structure consists of a checkerboardlike structure of oppositely charged particles and with the unit cell edge length $a \simeq \sqrt{2} a_{NN}$, where a_{NN} is the nearest neighbor (NN) distance between particles (approximately sum of half of the $D_{\rm H}$ of two individual constituents) of a PEGgrafted particle. On the other hand, Figure 2b shows a 1D diffraction pattern for the (A/B') structure with Bragg peaks that can be indexed by a $\sqrt{3} \times \sqrt{3}$ hexagonal lattice with $a \simeq$ 55 nm. This notation (i.e., $\sqrt{3} \times \sqrt{3}$) is used to indicate a hexagonal lattice with unit cell edge length $a \simeq \sqrt{3} a_{\rm NN}$ having a cell basis pseudoformula AB2'. Illustrated depictions of the two observed structures and their development by variation of pH are included as insets in Figure 2a,b and schematically in Figure 2a1,b1 (see rationalization of the DLS of particles in

Supporting Information). We note that the formation of single-orderly particles at pH 2 (depicted schematically in Figure 2a1,b1) is likely formed by the -COOH-grafted AuNPs (A' and A). This can be rationalized by the fact that collectively, the $-NH_2$ groups transform to $-NH_3^+$ at pH 2, and consequently, the whole particle is sufficiently water-soluble that it does not populate the surface.

Upon lowering the pH, the -COOH terminal particles get less charged by the transformation of -COO- groups to -COOH, while the -NH2 terminal group particles become more positively charged by transforming to -NH3+. Based on the ζ -potential values from Table 1, we estimate that the effective charge ratio of A' to B is greater than 1 at neutral pH. As the pH is lowered, there is a decrease in the net charge of A'and an increase in the net charge of B. This adjustment in charge distribution leads to an effective charge ratio that approaches 1, whereupon a neutral A'B checkerboard square lattice is formed. For the A/B' system, in contrast to the previous scenario, the relative charge ratio of A to B' is estimated to be approximately 3 based on the ζ -potential. As we decrease the pH, the effective charge distribution on these two species converges to a ratio of 2, whereupon an AB_2 ' hexagonal lattice is formed. More details on ζ -potential values at different pH values can be found in the Supporting Information Table S1.

To corroborate and complement the nominal structures deduced from GISAXS, XR experiments on the same samples under the exact same conditions have been performed. The analysis of the XR provided the characteristic thickness of the film and the surface density of AuNPs. Figure S11 in the Supporting Information shows normalized XR scans and the corresponding extracted ED profiles. The bell-shaped peak in the ED profiles represents the excess ED due to the AuNP film, confirming a single layer of the constituent AuNPs, i.e., 5 and 10 nm. As shown in the Supporting Information Table S3, the surface densities of AuNPs are consistent with the above GISAXS analysis. This shows that the XR properly estimates the pseudostoichiometry of the ionic-like crystals at the interface. The experiments shown in Figure 2 demonstrate

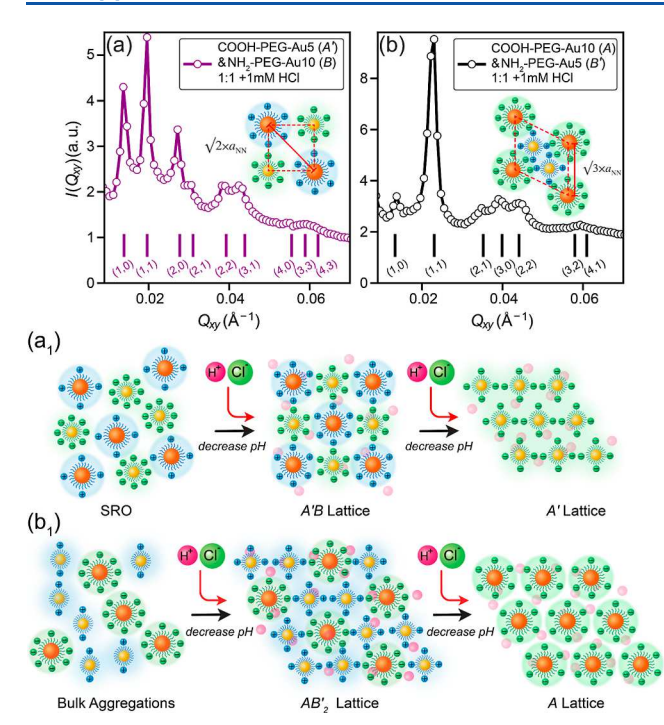


Figure 2. Formation of 2D checkerboard-like and hexagonal lattices of binary charged mixtures tuned by the effective surfacecharge density. GISAXS line-cut profiles of an equimolar mixture of (a) A' and B and (b) A and B' at 1 mM HCl. Vertical bars represent the calculated peak positions for the corresponding lattices with the respective Miller indices mentioned below. Insets depict ideal lattices (refer to Table 1 for key notations). (a1,b1) show the schematic illustration of lattice transitions with the addition of HCl (depicted by the red arrows). The HCl addition is dynamic and done in-situ. At a given pH (pH = 3), the mixture of A' and B forms a $\sqrt{2} \times \sqrt{2}$ square lattice structure. By interchanging the core diameters of AuNPs, the system changes from a square lattice to a $\sqrt{3}$ \times $\sqrt{3}$ hexagonal lattice due to the differences in total surface charge, which are dominated by the surface area of each particle. On further lowering the pH (pH 2), the surface is occupied with the -COOH-terminated particles due to an increase in the solubility of the $-NH_2$ -terminated particles.

control over the constituents' total charge by manipulating the pH. Below, we show that the same and other superstructures can be formed by manipulating the mixing ratio of the various constituents.

3.2. Bulk Mixing-Ratios-Induced Superstructures. As previously demonstrated, the formation of a more exotic structure is observed at a pH of 3. Consequently, we delve into a more comprehensive exploration of the influence exerted by the bulk mixing ratios at this specific pH level. Figure 3 shows the GISAXS profiles of the A'/B and A/B' systems at different molar mixing ratios for a fixed pH of 3. Figure 3a shows a diffraction pattern from a 2:1 molar mixing ratio of A'/B that is consistent with the formation of a $\sqrt{3} \times \sqrt{3}$ hexagonal structure. The unit cell of this structure is similar to the one depicted in Figure 2b, but with a pseudostoichiometric formula of $A_2'B$ in contrast to AB_2' . We note that the lattice constant for the AB_2 ' structure in Figure 2b $a \simeq 55$ nm, but for A_2 'B in Figure 3a $a \simeq 49$ nm, which is consistent with the Coulombic repulsion between the B' particles since at the specified pH, the two B' particles within the AB_2' unit cell maintain a high charge. This leads them to repel each other, causing the formation of a unit cell marginally larger than that observed for $A_2'B$. This disparity can be linked to the two A' particles,

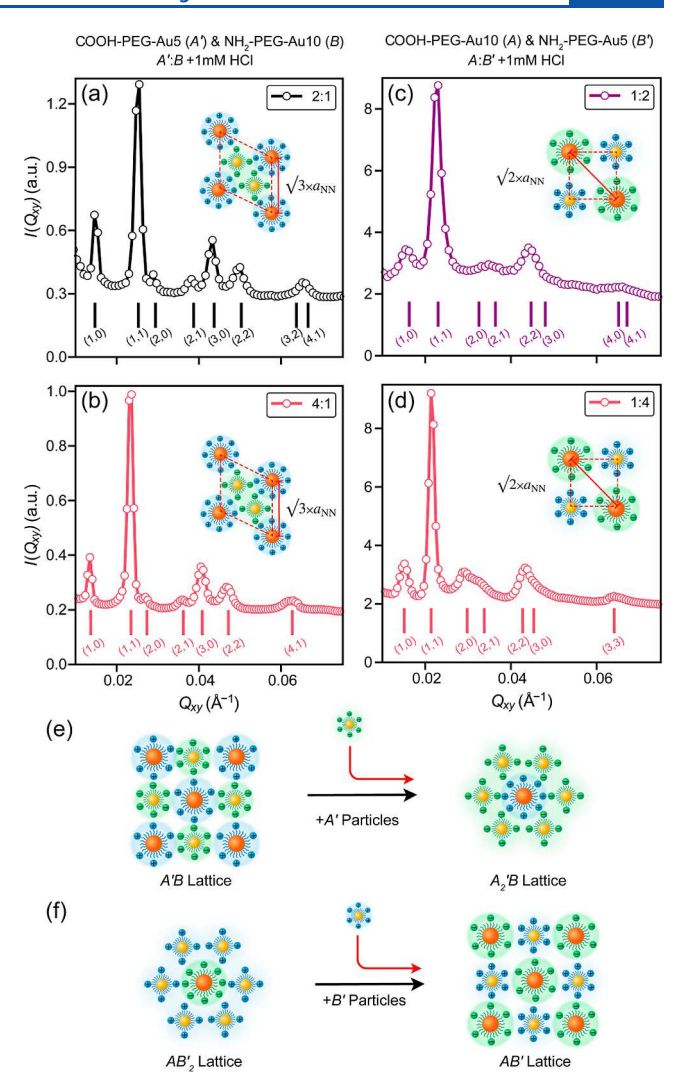


Figure 3. Mixing-ratio-induced lattice transitions from an A'B square lattice to an A2'B hexagonal lattice and from an AB2' hexagonal lattice to an AB' hexagonal lattice. GISAXS line-cut profiles and schematic lattice representations of binary mixtures of A' and B at (a) 2:1 and (b) 4:1 molar ratios, and binary mixtures of A and B' at (c) 1:2 and (d) 1:4 molar ratios, at 1 mM HCl as indicated. Insets depict ideal lattices (refer to Table 1 for key notations). Vertical bars represent the calculated peak positions for the corresponding lattices with their respective Miller indices mentioned below. (e,f) Schematic illustration of lattice transitions. At a given pH (pH = 3), the equimolar mixture of A'/B forms a 2D $\sqrt{2} \times \sqrt{2}$ A'B square lattice (Figure 2a). The red arrows indicate the addition of 5 nm particles, which was performed externally and solely for illustrative purposes. On further increasing the molar ratio to 2:1, the lattice transforms to a $\sqrt{3} \times \sqrt{3} A_2'B$ hexagonal lattice, which remains unchanged at a 4:1 molar ratio, indicating the structural resistance to increasing ratios. Similarly, the equimolar mixture of A/B' forms a 2D $\sqrt{3} \times \sqrt{3} AB_2'$ hexagonal lattice (Figure 2b). By further increasing the molar ratio to 1:2, the lattice transforms to a $\sqrt{2} \times \sqrt{2} AB'$ square lattice, which remains unchanged at a 1:4 molar ratio. These results emphasize the tunability of lattice structures in binary mixtures, showcasing their structural robustness.

which display an almost neutral charge state. This $A_2'B$ structure is also corroborated by XR analysis, as discussed in reference to Figure 2a and in the Supporting Information. As noted above, a 1:1 mixing ratio of the same A'/B constituents leads to the formation of a $\sqrt{2} \times \sqrt{2}$ square lattice. As the

molar ratio is increased (by increasing the amount of the A' constituent), the system undergoes a transition from a square lattice to a hexagonal lattice, and this hexagonal lattice remains robust as the molar ratio is further increased to 4:1. Similarly, Figure 3c shows the formation of a $\sqrt{2} \times \sqrt{2}$ square-lattice originating from the 1:2 mixture of A/B' constituents. The unit cell of this structure is similar to the one mentioned in Figure 2a but has a pseudostoichiometric formula of AB' due to its individual constituents. Figure 3 shows the formation of a similar AB' square lattice with an increase in the molar mixing ratio to 1:4 from 1:2, indicating the robustness of the square lattice with the increase in mixing ratios. Unlike the earlier case of the A'/B system, in the A/B' system, the transition from a 1:1 ratio leads to a change from a $\sqrt{3} \times \sqrt{3}$ hexagonal lattice to a $\sqrt{2} \times \sqrt{2}$ square lattice.

A central conclusion from the present and previous sections is that the surface charge density created by the -COOH group is larger than that of the $-\text{NH}_2$ terminal group, consistent with ζ -potential values and published results. Also, the total charge on each particle scales with the surface area of the core. These differences can be taken advantage of by manipulating the pH in the suspension to vary the net surface charge. Next, we present the effect of varying the pH on the crystallization of the same system with fixed molar mixing ratios.

3.3. pH-Controlled Superstructures. Figure 4 shows the GISAXS measurements of A'/B at a 2:1 molar ratio at four different pH values. At neutral pH, the system spontaneously forms a checkerboard crystal structure with a relatively large lattice constant of $a \simeq 51$ nm, which is depicted schematically in the inset. Such a large lattice constant is unusual for a LRO of a neutral 5 kDa PEG/AuNP system. 14 To rationalize this, we note that previous results indicate that the -NH2 (B particles)-terminated particles spontaneously populate the surface due to a lower positive surface charge, while the -COOH (A' particles)-terminated particles carry a higher total negative charge density.³⁰ This results in a repulsion between the A' particles, leading to the increased unit cell size, as depicted schematically by a halo of the A' particles with an enlarged effective cross-section. To counteract this effect, we add HCl to the system, which balances the net charge on A' and B particles, and as a result, the lattice constant is reduced by \sim 20% to $a \simeq 43$ nm, as deduced from the diffraction patterns in Figure 4a,b. Consistently, decreasing the pH increases the propensity of A' particles to populate the surface as the B particles become more soluble due to an increase in positive charge density. Here, we note the relative enrichment of A' particles at the interface, compelling the system to settle into a pseudostoichiometric $A_2'B$ hexagonal unit cell, as extracted from Figure 4c and shown schematically in the inset. This formulation suggests the occupation of relatively two surface-rich A' particles in coordination with each B particle. To validate the proposed pseudostoichiometry of the emergent nominal structures, we conducted a thorough XR analysis on the aforementioned samples. The findings from this analysis are summarized in Figure S15. A summary of the average surface coverage, as inferred from XR with that derived from GISAXS, is presented in Figure S15 and Table S3. Remarkably, at pH 3, the computed surface coverage of the $A_2'B$ structure aligns perfectly with the coverage inferred from XR profiles. This concurrence unequivocally corroborates our proposed pseudostoichiometry $A_2'B$, thereby underscoring its relevance

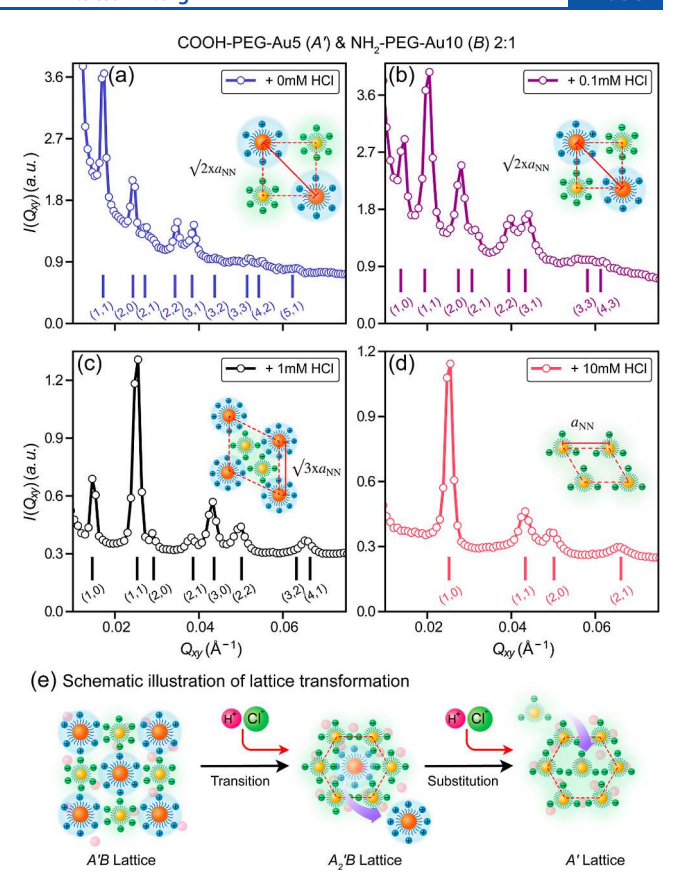


Figure 4. pH-induced symmetry transition in a 2:1 mixture of COOH–PEG–Au5 and NH₂–PEG–Au10. GISAXS line-cut profiles and schematic lattice representations of a binary mixture of A' and B at a 1:2 molar ratio at (a) 0, (b) 0.1, (c) 1, and (d) 10 mM HCl molar concentrations. Insets depict ideal lattices (refer to Table 1 for key notations). Vertical bars represent the calculated peak positions for the corresponding lattices with their respective Miller indices mentioned below. The mixture forms a 2D $\sqrt{2} \times \sqrt{2}$ square lattice at [HCl] = 0.1 mM and transforms to a $\sqrt{3} \times \sqrt{3}$ hexagonal lattice at [HCl] = 1 mM and further to a 1 × 1 hexagonal lattices. The HCl addition is dynamic and done *in-situ*. (e) represents a schematic illustration of lattice transformation from a $\sqrt{2} \times \sqrt{2}$ square lattice to a $\sqrt{3} \times \sqrt{3}$ hexagonal lattice and further to a 1 × 1 hexagonal lattice (the HCl addition is depicted by the red arrows).

and validity in this system. This trend of lowering the charge on the -COOH group of A' particles continues by lowering the pH and finally leading to a simple hexagonal structure consisting of the A' particles, as shown in the diffraction pattern and depicted in Figure 4d.³⁰ We rationalize that the surface predominance of particles A' can be attributed to the enriched charge density of particle B, which potentially augments its solubility, thereby encouraging their bulk presence. To summarize, the effect of lowering the pH and the progression of structural transitions are conceptually illustrated in Figure 4e.

4. CONCLUSIONS

In this study, we control the total surface charge of PEG-grafted AuNPs by adding carboxylic or amine terminal groups and by varying the pH. Based on previous results and ζ -potential measurements, we expect the carboxylic group to be negatively charged and the amine group to be positively

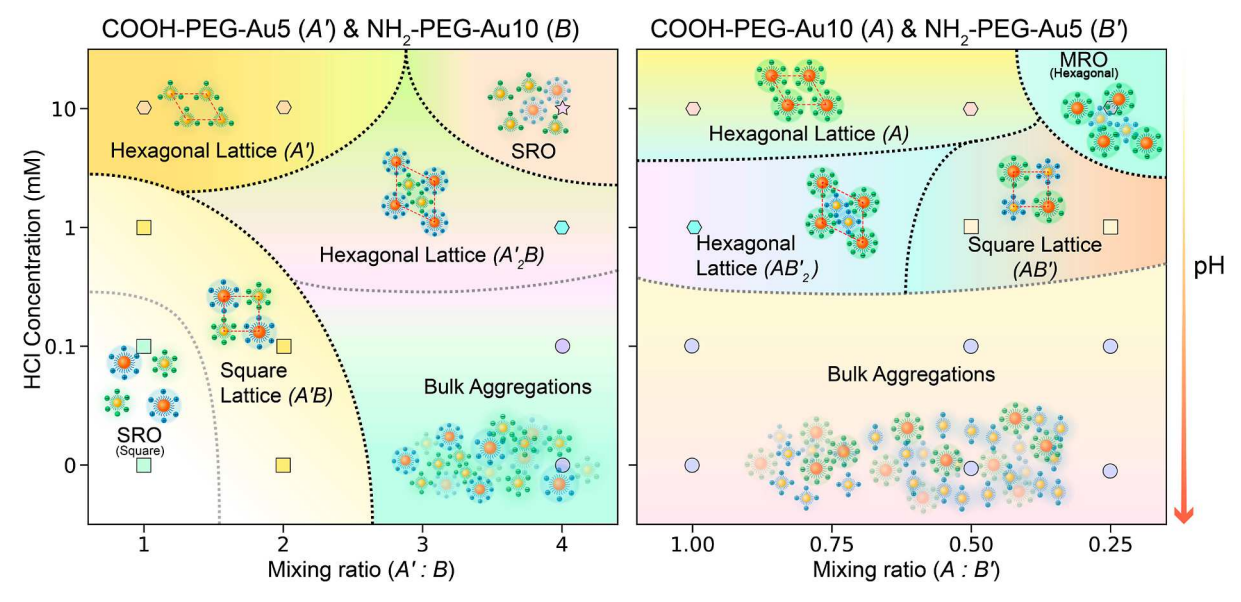


Figure 5. Schematic phase diagram of all structures reported in Table 2. The left pannel shows a schematic phase diagram of a binary mixture of A' and B', and the right pannel shows a schematic phase diagram of a binary mixture of A' and B' as a function of the molar mixing ratio and HCl concentration. The axes are not to be scaled, and the phase boundaries are hypothetical. The markers refer to the experimental data points. The phase colors used are for aesthetic purposes only.

charged. Previous experiments³⁰ and ζ -potential measurements (see Table 1) have shown that at near-neutral pH, -COOH groups are negatively charged by deprotonating into -COO-, resulting in the grafted AuNPs being fully dispersed in the suspension. By contrast, the -NH2-terminated AuNPs are near charge-neutral, making them spontaneously migrate to the vapor/liquid interface at near-neutral pH.30 It has been observed that for charge-neutral particles, the primary driving force is attributed to the morphological changes in the PEGcorona and its hydrophobic properties.³⁶ Therefore, in order to take advantage of ordering by Coulombic interactions, we controlled the pH of the suspension and manipulated the charges of both end groups. In general, our results show that lowering the pH reduces the total charge in the -COOHterminated AuNPs and increases the total charge in the -NH₂terminated AuNPs. Our ζ -potential measurements confirm this finding (see Table S1) and provide a quick path for predicting the possible structures of such BNSLs. Using surface-sensitive X-ray diffraction techniques (GISAXS and XR), we tested the above hypotheses and determined the actual structures of AuNPs under various conditions. The main results of our study are summarized in a pH-mixing-ratios phase diagram in Figure 5 and are as follows: (1) a checkerboard square lattice can be achieved by either lowering the pH and/or manipulating molar mixing ratios. (2) By further lowering the pH or increasing the molar ratio, the system transforms from a checkerboard structure to a hexagonal structure with a pseudostoichiometry of A'B and AB' to $A_2'B$ and AB_2' . This tunability enables the tailoring of material properties by manipulating the molar ratios of the constituents. (3) In the extreme case of low pH, one of the constituents (likely, COOH-terminated PEG-AuNPs) forms a single-particle hexagonal structure akin to neutral PEG-grafted AuNP structures at the vapor/liquid interface. Our study elucidates self-assembly mechanisms that organize nanostructures through bottom-up approaches, offering promising pathways for potential applications in photonics and plasmonics.

ASSOCIATED CONTENT

Data Availability Statement

The findings of this study are supported by data found within the article and the provided <u>Supporting Information</u>. Further relevant information and source data can be obtained from the corresponding author upon making a reasonable request.

Supporting Information

The Supporting Information is available free of charge at https://pubs.acs.org/doi/10.1021/acsanm.3c05566.

DLS and ζ -potential measurements; 2D GISAXS data; control experiments of individual AuNPs; crystallographic calculations; additional GISAXS data; and XRR analysis (PDF)

AUTHOR INFORMATION

Corresponding Authors

Surya K. Mallapragada — Ames National Laboratory, and Department of Chemical and Biological Engineering, Iowa State University, Ames, Iowa 50011, United States; orcid.org/0000-0002-9482-7273; Email: suryakm@iastate.edu

Wenjie Wang — Division of Materials Sciences and Engineering, Ames National Laboratory, Ames, Iowa 50011, United States; orcid.org/0000-0002-7079-1691; Email: wenjiew@ameslab.gov

Authors

Binay P. Nayak — Ames National Laboratory, and Department of Chemical and Biological Engineering, Iowa State University, Ames, Iowa 50011, United States; orcid.org/0000-0002-3995-4114

Honghu Zhang — National Synchrotron Light Source-II, Brookhaven National Laboratory, Upton, New York 11973, United States; orcid.org/0000-0003-1784-7825

Wei Bu - NSF's ChemMatCARS, Pritzker School of Molecular Engineering, University of Chicago, Chicago, Illinois 60637, United States; o orcid.org/0000-0002-9996-3733

Benjamin M. Ocko — National Synchrotron Light Source-II, Brookhaven National Laboratory, Upton, New York 11973, United States; Occid.org/0000-0003-2596-1206

Alex Travesset — Ames National Laboratory, and Department of Physics and Astronomy, Iowa State University, Ames, Iowa 50011, United States; orcid.org/0000-0001-7030-9570

David Vaknin — Ames National Laboratory, and Department of Physics and Astronomy, Iowa State University, Ames, Iowa 50011, United States; orcid.org/0000-0002-0899-9248

Complete contact information is available at: https://pubs.acs.org/10.1021/acsanm.3c05566

Author Contributions

W.W., D.V., and S.M. conceived and supervised the project. B.N., D.V., and W.W. designed and conducted the experiments and analyzed the data. B.N., W.W., and D.V. wrote the manuscript. B.M.O., W.B., and H.Z. provided support in X-ray scattering experiments, data acquisition, and data processing. A.T. provided theoretical inputs. S.M., D.V., and W.W. secured the funding for the project. All coauthors read and reviewed the manuscript.

Notes

The authors declare no competing financial interest.

ACKNOWLEDGMENTS

The authors would like to thank Hyeong Jin Kim for initiating this work at Ames National Laboratory. The research was supported by the U.S. Department of Energy (U.S. DOE), Office of Basic Energy Sciences, Division of Materials Sciences and Engineering. Iowa State University operates Ames National Laboratory for the U.S. DOE under contract no. DE-AC02-07CH11358. Part of this research used the Open Platform Liquid Surfaces (OPLS) end station of the Soft Matter Interfaces Beamline (SMI, Beamline 12-ID) at the National Synchrotron Light Source II, a U.S. Department of Energy (DOE) Office of Science User Facility operated for the DOE Office of Science by Brookhaven National Laboratory under contract no. DE-SC0012704. Part of this research used NSF's ChemMatCARS Sector 15. NSF's ChemMatCARS Sector 15 is supported by the Divisions of Chemistry (CHE) and Materials Research (DMR), National Science Foundation, under grant no. NSF/CHE-1834750. The use of the Advanced Photon Source, an Office of Science User Facility operated for the U.S. Department of Energy (DOE) Office of Science by Argonne National Laboratory, was supported by the U.S. DOE under contract no. DE-AC02-06CH11357.

REFERENCES

- (1) Talapin, D. V.; Lee, J.-S.; Kovalenko, M. V.; Shevchenko, E. V. Prospects of colloidal nanocrystals for electronic and optoelectronic applications. *Chem. Rev.* **2010**, *110*, 389–458.
- (2) Sung, J.; Jo, P. S.; Shin, H.; Huh, J.; Min, B. G.; Kim, D. H.; Park, C. Transparent, Low-Electric-Resistance Nanocomposites of Self-Assembled Block Copolymers and SWNTs. *Adv. Mater.* **2008**, *20*, 1505–1510.
- (3) Fan, J. A.; Wu, C.; Bao, K.; Bao, J.; Bardhan, R.; Halas, N. J.; Manoharan, V. N.; Nordlander, P.; Shvets, G.; Capasso, F. Self-assembled plasmonic nanoparticle clusters. *science* **2010**, 328, 1135–1138.
- (4) Tao, A.; Sinsermsuksakul, P.; Yang, P. Tunable plasmonic lattices of silver nanocrystals. *Nat. Nanotechnol.* **2007**, *2*, 435–440.

- (5) Kim, H. J.; Wang, W.; Bu, W.; Mallapragada, S. K.; Vaknin, D. Lamellar and Hexagonal Assemblies of PEG-Grafted Silver Nanoparticles: Implications for Plasmonics and Photonics. *ACS Appl. Nano Mater.* **2022**, *5*, 17556–17564.
- (6) Yadav, A.; Gerislioglu, B.; Ahmadivand, A.; Kaushik, A.; Cheng, G. J.; Ouyang, Z.; Wang, Q.; Yadav, V. S.; Mishra, Y. K.; Wu, Y.; et al. Controlled self-assembly of plasmon-based photonic nanocrystals for high performance photonic technologies. *Nano Today* **2021**, *37*, 101072.
- (7) Yazdani, N.; Jansen, M.; Bozyigit, D.; Lin, W. M.; Volk, S.; Yarema, O.; Yarema, M.; Juranyi, F.; Huber, S. D.; Wood, V. Nanocrystal superlattices as phonon-engineered solids and acoustic metamaterials. *Nat. Commun.* **2019**, *10*, 4236.
- (8) Yu, C.; Guo, X.; Muzzio, M.; Seto, C. T.; Sun, S. Self-Assembly of Nanoparticles into Two-Dimensional Arrays for Catalytic Applications. *ChemPhysChem* **2019**, *20*, 23–30.
- (9) Gajraj, V.; Devi, P.; Kumar, R.; Sundriyal, N.; Reddy, M.; Mariappan, C. Self-assembly of novel cobalt iron phosphate nanoparticles for the solid-state supercapattery and high-performance hydrogen evolution reaction. *Int. J. Hydrogen Energy* **2023**, 48, 17868–17881.
- (10) Wang, D.; Kou, R.; Choi, D.; Yang, Z.; Nie, Z.; Li, J.; Saraf, L. V.; Hu, D.; Zhang, J.; Graff, G. L.; et al. Ternary self-assembly of ordered metal oxide- graphene nanocomposites for electrochemical energy storage. *ACS Nano* **2010**, *4*, 1587–1595.
- (11) Pomerantseva, E.; Bonaccorso, F.; Feng, X.; Cui, Y.; Gogotsi, Y. Energy storage: The future enabled by nanomaterials. *Science* **2019**, 366, No. eaan8285.
- (12) Urban, J. J.; Talapin, D. V.; Shevchenko, E. V.; Kagan, C. R.; Murray, C. B. Synergism in binary nanocrystal superlattices leads to enhanced p-type conductivity in self-assembled PbTe/Ag2Te thin films. *Nat. Mater.* **2007**, *6*, 115–121.
- (13) Dong, A.; Chen, J.; Vora, P. M.; Kikkawa, J. M.; Murray, C. B. Binary nanocrystal superlattice membranes self-assembled at the liquid—air interface. *Nature* **2010**, *466*, 474—477.
- (14) Kim, H. J.; Wang, W.; Zhang, H.; Freychet, G.; Ocko, B. M.; Travesset, A.; Mallapragada, S. K.; Vaknin, D. Binary superlattices of gold nanoparticles in two dimensions. *J. Phys. Chem. Lett.* **2022**, *13*, 3424–3430.
- (15) Deng, K.; Xu, L.; Guo, X.; Wu, X.; Liu, Y.; Zhu, Z.; Li, Q.; Zhan, Q.; Li, C.; Quan, Z. Binary nanoparticle superlattices for plasmonically modulating upconversion luminescence. *Small* **2020**, *16*, 2002066.
- (16) Ye, X.; Chen, J.; Diroll, B. T.; Murray, C. B. Tunable plasmonic coupling in self-assembled binary nanocrystal superlattices studied by correlated optical microspectrophotometry and electron microscopy. *Nano Lett.* **2013**, *13*, 1291–1297.
- (17) Shevchenko, E. V.; Talapin, D. V.; O'brien, S.; Murray, C. B. Polymorphism in AB13 nanoparticle superlattices: an example of semiconductor- metal metamaterials. *J. Am. Chem. Soc.* **2005**, *127*, 8741–8747.
- (18) Feng, W.; Wang, L.; Xu, X.; Zhang, X.; Lin, S. Self-Assembly of ABC-Type Patchy Nanoparticles Formed by Crosslinking Triblock Copolymer Micelles. *Giant* **2023**, *15*, 100174.
- (19) Yu, Q.; Chen, J.; Shi, D.; Chen, M. Ordered self-assembly of DNA-modified nanoparticles in salt solutions. *Colloids Surf., A* **2023**, 671, 131669.
- (20) Macfarlane, R. J.; Lee, B.; Jones, M. R.; Harris, N.; Schatz, G. C.; Mirkin, C. A. Nanoparticle superlattice engineering with DNA. *Science* **2011**, 334, 204–208.
- (21) Kalsin, A. M.; Fialkowski, M.; Paszewski, M.; Smoukov, S. K.; Bishop, K. J.; Grzybowski, B. A. Electrostatic self-assembly of binary nanoparticle crystals with a diamond-like lattice. *Science* **2006**, *312*, 420–424.
- (22) Wang, K.; Li, F.; Jin, S.-M.; Wang, K.; Tian, D.; Hussain, M.; Xu, J.; Zhang, L.; Liao, Y.; Lee, E.; et al. Chain-length effect on binary superlattices of polymer-tethered nanoparticles. *Mater. Chem. Front.* **2020**, *4*, 2089–2095.

- (23) Kostiainen, M. A.; Hiekkataipale, P.; Laiho, A.; Lemieux, V.; Seitsonen, J.; Ruokolainen, J.; Ceci, P. Electrostatic assembly of binary nanoparticle superlattices using protein cages. *Nat. Nanotechnol.* **2013**, *8*, 52–56.
- (24) Ha, J.-M.; Lim, S.-H.; Dey, J.; Lee, S.-J.; Lee, M.-J.; Kang, S.-H.; Jin, K. S.; Choi, S.-M. Micelle-assisted formation of nanoparticle superlattices and thermally reversible symmetry transitions. *Nano Lett.* **2019**, *19*, 2313–2321.
- (25) Dey, J.; Lee, S.-J.; Kim, J.; Lim, S.-H.; Ha, J.-M.; Lee, M.-J.; Choi, S.-M. Spontaneous Formation of Highly Stable Nanoparticle Supercrystals Driven by a Covalent Bonding Interaction. *Nano Lett.* **2021**, *21*, 258–264.
- (26) Ye, X.; Zhu, C.; Ercius, P.; Raja, S. N.; He, B.; Jones, M. R.; Hauwiller, M. R.; Liu, Y.; Xu, T.; Alivisatos, A. P. Structural diversity in binary superlattices self-assembled from polymer-grafted nanocrystals. *Nat. Commun.* **2015**, *6*, 10052.
- (27) Bian, T.; Gardin, A.; Gemen, J.; Houben, L.; Perego, C.; Lee, B.; Elad, N.; Chu, Z.; Pavan, G. M.; Klajn, R. Electrostatic coassembly of nanoparticles with oppositely charged small molecules into static and dynamic superstructures. *Nat. Chem.* **2021**, *13*, 940–949.
- (28) Liljestrom, V.; Seitsonen, J.; Kostiainen, M. A. Electrostatic self-assembly of soft matter nanoparticle cocrystals with tunable lattice parameters. *ACS Nano* **2015**, *9*, 11278–11285.
- (29) Wang, D.; Nap, R. J.; Lagzi, I.; Kowalczyk, B.; Han, S.; Grzybowski, B. A.; Szleifer, I. How and why nanoparticle's curvature regulates the apparent pK_a of the coating ligands. *J. Am. Chem. Soc.* **2011**, 133, 2192–2197.
- (30) Kim, H. J.; Nayak, B. P.; Zhang, H.; Ocko, B. M.; Travesset, A.; Vaknin, D.; Mallapragada, S. K.; Wang, W. Two-dimensional assembly of gold nanoparticles grafted with charged-end-group polymers. J. Colloid Interface Sci. 2023, 650, 1941–1948.
- (31) Doane, T. L.; Cheng, Y.; Babar, A.; Hill, R. J.; Burda, C. Electrophoretic Mobilities of PEGylated Gold NPs. *J. Am. Chem. Soc.* **2010**, *1*32, 15624–15631.
- (32) Wang, W.; Zhang, H.; Kuzmenko, I.; Mallapragada, S.; Vaknin, D. Assembling bare Au nanoparticles at positively charged templates. *Sci. Rep.* **2016**, *6*, 26462–26469.
- (33) Zhang, H.; Nayak, S.; Wang, W.; Mallapragada, S.; Vaknin, D. Interfacial self-assembly of polyelectrolyte-capped gold nanoparticles. *Langmuir* **2017**, 33, 12227–12234.
- (34) Zhang, H.; Wang, W.; Akinc, M.; Mallapragada, S.; Travesset, A.; Vaknin, D. Assembling and ordering polymer-grafted nanoparticles in three dimensions. *Nanoscale* **2017**, *9*, 8710–8715.
- (35) Kim, H. J.; Hossen, M. M.; Hillier, A. C.; Vaknin, D.; Mallapragada, S. K.; Wang, W. Interfacial and bulk assembly of anisotropic gold nanostructures: implications for photonics and plasmonics. ACS Appl. Nano Mater. 2020, 3, 8216–8223.
- (36) Zhang, H.; Wang, W.; Mallapragada, S.; Travesset, A.; Vaknin, D. Macroscopic and Tunable Nanoparticle Superlattices. *Nanoscale* **2017**, *9*, 164–171.
- (37) Nayak, B. P.; Kim, H. J.; Travesset, A.; Vaknin, D.; Mallapragada, S. K.; Wang, W. Tuning Self-Assembly of Gold Nanoparticles Grafted with Charged Polymers by Varying Temperature and Electrolytes. *J. Phys. Chem. C* **2023**, 127, 24651–24657.
- (38) Pershan, P. S.; Schlossman, M. Liquid Surfaces and Interfaces: Synchrotron X-Ray Methods; Cambridge University Press, 2012.
- (39) Nayak, B. P.; Kim, H. J.; Nayak, S.; Wang, W.; Bu, W.; Mallapragada, S. K.; Vaknin, D. Assembling PNIPAM-Capped Gold Nanoparticles in Aqueous Solutions. *ACS Macro Lett.* **2023**, *12*, 1659–1664.
- (40) Als-Nielsen, J.; Desmond, M. Elements of Modern X-Ray Physics, 2nd ed.; Wiley, 2011.
- (41) Kim, H. J.; Wang, W.; Zhang, H.; Freychet, G.; Ocko, B. M.; Travesset, A.; Mallapragada, S. K.; Vaknin, D. Effect of polymer chain length on the superlattice assembly of functionalized gold nanoparticles. *Langmuir* **2021**, *37*, 10143–10149.